JAMES | Journal of Advances in Modeling Earth Systems

RESEARCH ARTICLE
10.1029/2022MS003070

Special Section:
The NASA GISS contribution to CMIP6

The Turning Point of the Aerosol Era

Susanne E. Bauer[1], Kostas Tsigaridis[1,2], Greg Faluvegi[1,2], Larissa Nazarenko[1,2], Ron L. Miller[1], Maxwell Kelley[1], and Gavin Schmidt[1]

[1]NASA Goddard Institute for Space Studies, New York, NY, USA, [2]Center for Climate Systems Research, Columbia University, New York, NY, USA

Key Points:

- Aerosol forcing in the Goddard Institute for Space Studies model reached its turning point in the first decade of the 21st century
- Non-linear aerosol-cloud forcing dominates in magnitude over aerosol direct forcing and pinpoint the timing of the turning point
- Within the next 25 years, global aerosol forcing might balance only 0%–20% of greenhouse gas forcing, compared to 80% in 1980–1990

Supporting Information:

Supporting Information may be found in the online version of this article.

Correspondence to:

S. E. Bauer,
Susanne.E.Bauer@NASA.gov

Citation:

Bauer, S. E., Tsigaridis, K., Faluvegi, G., Nazarenko, L., Miller, R. L., Kelley, M., & Schmidt, G. (2022). The turning point of the aerosol era. *Journal of Advances in Modeling Earth Systems*, *14*, e2022MS003070. https://doi.org/10.1029/2022MS003070

Received 8 MAR 2022
Accepted 11 DEC 2022

Author Contributions:

Conceptualization: Susanne E. Bauer
Data curation: Larissa Nazarenko
Formal analysis: Susanne E. Bauer
Investigation: Susanne E. Bauer
Methodology: Susanne E. Bauer, Kostas Tsigaridis

Abstract Over the CMIP6 historical period (1850–2014), aerosols provided the largest negative forcing compared to all other climate forcings via their ability to absorb or scatter solar radiation and alter clouds. Aerosols played an important role in counterbalancing warming by greenhouse gases (GHGs). Here we study aerosol forcing trends in the CMIP6 simulations of the NASA Goddard Institute for Space Studies (GISS) ocean-atmosphere ModelE version 2.1 (GISS-E2.1-G) using a fully coupled atmospheric composition configuration, including interactive gas-phase chemistry, and either an aerosol microphysical (MATRIX) or a mass-based aerosol (OMA) module. Simulations of the CMIP6 historical period are analyzed as well as four Shared Socioeconomic Pathway (SSP) future scenarios for 2015–2100: SSP1-2.6, SSP2-4.5, SSP3-7.0, and SSP5-8.5. The main conclusion of this study is that aerosol forcing in the GISS model has reached its turning point, switching from globally increasing to a decreasing trend in the first decade of the 21st century. This result is robust, independent of which aerosol module or SSP scenario is used. Non-linear aerosol-cloud interactions dominate as a forcing agent over aerosol-radiation interactions. Aerosols' ability to counterbalance GHG forcing on the global scale is today at a level comparable to that at the beginning of the last century. In the 1980s, the decade of largest global aerosol loads, aerosols balanced up to 80% of GHG forcing. As a consequence, global warming of the last decades, which is primarily driven by greenhouse gases, has been augmented by the effect of decreasing aerosol cooling in our model. By the end of this century, following the SSP scenarios, aerosols will only counterbalance 0%–20% of GHG forcing, depending on model and on scenario.

Plain Language Summary Climate change is the result of the aggregate effect of a number of individual forcing agents changing the radiative balance at the top of the atmosphere over time. As a result, if positive radiative forcings dominate over negative forcings, the Earth's surface warms. Over the historical period, since the pre-industrial era, greenhouse gases (GHG) and aerosol have provided the largest positive and negative forcings, respectively. However, the relationship between GHG and aerosols have rapidly changed in the last decades, and future projections show much more dramatic dominance of GHG over aerosols. This study investigates the connection between emissions, atmospheric composition and climate forcing. We find that aerosols' ability to counterbalance GHG forcing reached its maximum effect in the 1980s, and that since the first decade of the 21st century, aerosol effects are globally on a decreasing trajectory. Reduced aerosol loads are important for health, but accelerate global warming, in the absence of concurrent GHG reductions. The results presented here are based upon the NASA GISS climate model, and the four future scenarios used. These scenarios are not intended as predictions, but represent a range of possible changes in atmospheric composition (including greenhouse gases) based on differing assumptions about future energy policies.

1. Introduction

Assessing regional and global trends in aerosol forcing under past and future climate projections is crucial to improve our understanding of past and future climate change (Arias et al., 2021; Hansen et al., 1998). The Coupled Model Intercomparison Project Phase 6 (CMIP6) (Eyring et al., 2016) provides forcing and emission estimates for the historical period, 1750–2014 (Hoesly et al., 2018), and sets of future emission scenarios (Feng et al., 2020; Gidden et al., 2019; Meinshausen et al., 2020; O'Neill et al., 2016) that span from 2015 until 2300, covering multiple pathways of possible future socio-economic developments.

Calculating and understanding aerosol trends is complicated, as their time evolution depends on numerous natural and anthropogenic sources emitting various types of gaseous aerosol precursor and aerosol species that change in time and space. Translating emissions into concentrations and eventually forcings that act on the climate system

Software: Susanne E. Bauer, Greg Faluvegi, Maxwell Kelley
Validation: Susanne E. Bauer
Visualization: Susanne E. Bauer
Writing – original draft: Susanne E. Bauer
Writing – review & editing: Susanne E. Bauer, Kostas Tsigaridis, Ron L. Miller, Gavin Schmidt

in various ways such as aerosol direct (RFari) and aerosol effects on clouds (RFaci) is a complex task, which adds uncertainty in the estimates of aerosol impacts on climate.

Trends in aerosol emissions have been driven by industrialization and modernization of technology. Industrialization, which relies on the use of fossil fuel energy, has had a significant impact on the aerosol load, resulting in severe pollution episodes like the 1952 smog event in London (Bell et al., 2004). Starting in the 1970s in the USA and in Europe, mitigation measures were implemented (Turnock, 2016), and political change in the 1990s in Eastern Europe lead to the breakdown of many highly polluting industries, resulting in significant improvements in terms of aerosol loads and air quality. Agriculture is an emission sector that is strongly linked to population, and is one of the few sectors that experiences persistent growth. Modernizations of technologies have led to large changes over the past decades in industrialized countries and more recently in Asia (Ramachandran et al., 2020). Trends in aerosol composition and forcing have been studied in the past by modeling (Bauer et al., 2020; Mortier et al., 2020; Yang et al., 2018) and satellite studies (Subba et al., 2020; Zhao et al., 2017). Satellite measurements of Earth's energy imbalance found a significant positive trend in between 2001 and 2020 with an increase in 0.38 ± 0.24 Wm^{-2} $decade^{-1}$, which is attributed not only to aerosol (Raghuraman et al., 2021).

The IPCC Sixth Assessment Report (AR6) (Arias et al., 2021) acknowledges a recently decreasing trend in aerosol forcing since 2000. It is believed with high confidence that aerosol optical depth, derived from satellite- and ground-based radiometers, has decreased since 2000 over the mid-latitude continents of both hemispheres, but increased over South Asia and East Africa. Global carbonaceous aerosol budgets and trends remain poorly characterized, and the IPCC AR6 report only has low confidence in the finding of trends in BC and organic aerosol. Quaas et al. (2022) found robust evidence for the reversal in the aerosol effective climate forcing trend since 2000, based on satellite and remote sensing products of AOD, liquid water path (LWP), cloud droplet number concentration (CDNC), radiative fluxes, as well as CMIP6 models, including the NASA GISS model. Quaas et al. (2022) found clear, robust and consistent signals for net declining anthropogenic aerosol influence on climate since 2000, the period for which high-quality satellite retrievals are available.

Aerosols are just one of multiple forcing agents in the climate system. In order to understand the relevance of aerosol forcings, it is important to look at them in relation to all other forcings that change over time, due to both natural or anthropogenic causes. Over the past century, cooling by aerosol forcing has counterbalanced a substantial portion of the positive forcing by well-mixed GHGs. The regional and global balance between GHGs and short lived climate forcers is crucial in understanding future climate development and possible mitigation (Lund et al., 2020). Looking at the impact of single forcing experiments (Figure 1, setup explained in Section 2.2), it is clear that the trend in surface temperature is mainly driven by the counterbalance between GHG and aerosol forcing. All other forcings play a much smaller role. Ozone forcing, which is not included as a single forcing experiment, but is included in the all-drivers simulations, has an effective radiative forcing of 0.27 W/m^2 in the GISS model (Miller et al., 2021), and as such is the third most important climate forcing during the historical period, after GHG and aerosols. Over the past decades, the relationship between GHG and aerosol forcing has strongly changed, due to the consistently increasing GHG forcing, and the leveling off and possible globally decreasing effect of aerosol forcing on the climate system.

This study looks at the connections between composition and forcing. Our core question is whether we can pinpoint the timing of maximum aerosol forcing, when the trend turned from increasing to decreasing. Aerosols differ from GHG in their uniquely strong regional signature, and not all regions affect climate equally. We will study this period between 1850 and 2100 to understand: when and why are aerosol forcings changing? How are these changes projected in the SSPs? How does aerosol forcing offset GHG forcing? How does this compensation evolve with time and what are the implications for future warming?

2. Model Description

2.1. Historical and SSP Simulations

The model used is the NASA GISS ModelE, the version named GISS-E2.1-G in CMIP6. The climate model's physical parameterizations and satellite era climatology are described in Kelley et al. (2020), the transient historical simulation (1850–2014) in Miller et al. (2021) and the future scenario simulations from 2014 to 2100 are discussed in Nazarenko et al. (2022). The two aerosol schemes used here, MATRIX and OMA, and the model's performance during the historical period with regard to atmospheric composition for the observed ocean

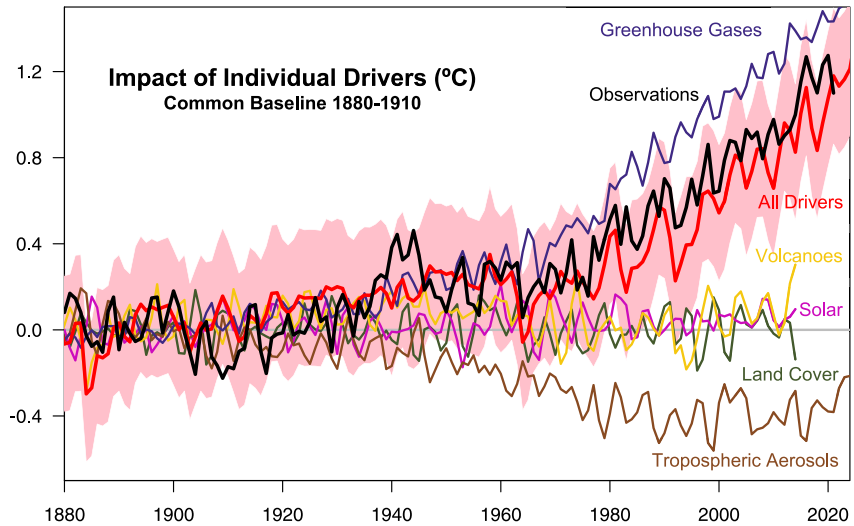

Figure 1. Global mean surface temperature (in °C) response in single and all-forcing runs. Five ensemble model simulations have been carried out only varying one forcing agent at a time. Single forcing runs were performed for GHG (blue), land cover changes (green), solar variability (pink), volcanic aerosols (yellow), and aerosol (brown). Observational data (black) are from GISTEMP. The mean of five ensembles is plotted, except for the "all drivers" simulations which includes 10 ensembles, the standard variability is marked in shading (red). Runs extended beyond 2014 are shown for SSP2-4.5. The post-eruption response is smaller in the Volcanic forcing run than the all-forcing run due to the smaller number of volcanic runs and internal variability that obscures the forced signal.

conditions is described and evaluated in Bauer et al. (2020). We examine here the coupled ocean-atmosphere historical experiments and four SSP future scenario simulations until 2100.

The horizontal and vertical resolution of the atmospheric component of ModelE2.1 is 2° in latitude by 2.5° in longitude with 40 vertical layers extending from the surface to 0.1 hPa near the stratopause. The ocean component of GISS-E2-1-G in the CMIP6 archive uses the GISS Ocean version 1 (GO1). GO1 has a horizontal resolution of 1° latitude by 1.25° longitude, and 40 vertical layers. Aerosols and ozone are calculated prognostically using either the One-Moment Aerosol (OMA) (Bauer et al., 2020) or the aerosol microphysical model MATRIX (Multiconfiguration Aerosol TRacker of mIXing state) (Bauer et al., 2008).

Both aerosol schemes are coupled to the tropospheric chemistry scheme (Shindell et al., 2001, 2003), which includes inorganic chemistry of O_x, NO_x, HO_x, CO, and organic chemistry of CH_4 and higher hydrocarbons using the CBM4 scheme (Gery et al., 1989), and the stratospheric chemistry scheme (Shindell et al., 2006) which includes chlorine and bromine chemistry together with polar stratospheric clouds.

MATRIX (Bauer & Menon, 2012; Bauer et al., 2008, 2010), is an aerosol microphysics scheme based on the quadrature method of moments. MATRIX represents new particle formation (the binary scheme [Vehkamäki et al., 2002] was chosen here), gas-particle mass transfer, aerosol-phase chemistry, condensational growth, and coagulation within and between particle populations. MATRIX is able to explicitly simulate the mixing state of aerosols (Bauer, Ault, & Prather, 2013). The amount of water in aerosol is calculated with the aerosol thermodynamics module EQSAM (Metzger et al., 2002), using the phase state of an ammonia-sulfate-nitrate-water inorganic aerosol in thermodynamic equilibrium for metastable aerosols, except for sea salt where the Lewis parameterization is used (Lewis & Schwartz, 2013). As such, hygroscopic swelling of aerosol is represented and does not need to be recalculated during the radiative calculations. Secondary organic aerosol (SOA) is parameterized as a source of non-volatile aerosol emitted directly from vegetation. A 10% yield from monoterpene emissions is assumed, which is added to the non-volatile organic aerosol fraction in the model, and remains indistinguishable from organic aerosols from other sources. MATRIX results presented here use mechanism M1 (Bauer et al., 2008) that tracks 16 mixing state classes, 51 aerosol tracers and resolves eight chemical components; sulfate, nitrate, ammonium, aerosol water, black carbon, organic carbon, sea salt and mineral dust. In MATRIX, the number of cloud activating particles is based on the aerosol activation parameterizations of Abdul-Razzak et al. (1998) and Abdul-Razzak and Ghan (2000), which treat multimodal and multicomponent aerosols and

provide the activated fraction of the number and mass concentration for each population, based on the population composition and the cloud updraft velocity. In MATRIX, all aerosol species can lead to cloud activation including dust, depending on its size and mixing state, however contributions from dust are minimal. Ice nucleation pathways are not included in this model version. ModelE2.1 includes only the first indirect effect, which is the effect of aerosols on cloud droplet number concentration (CDNC) and thereby on cloud albedo, cloud effective radii and radiation (Menon et al., 2008, 2010).

OMA (Bauer & Koch, 2005; Bauer, Koch, et al., 2007; Bauer, Mishchenko, et al., 2007; Bauer et al., 2020; Koch et al., 2006; Miller et al., 2006; Tsigaridis et al., 2013), is a mass-based scheme in which aerosols are externally mixed and (except for dust) assumed to have a prescribed constant size distribution. OMA transports 34 tracers. The following aerosol components are treated in this version: sulfate, nitrate, ammonium, carbonaceous aerosols (black carbon and organic carbon, including the NO_x-dependent formation of SOA and methanesulfonic acid formation [Tsigaridis & Kanakidou, 2007]), dust (including heterogeneous gas uptake on dust surfaces [Bauer & Koch, 2005]) and sea salt. SOA is formed from isoprene and terpenes. Terpene emissions have a seasonal but not interannual variability and do not respond to climate change, while isoprene emissions are calculated prognostically (Guenther et al., 1993), increasing in a warmer climate (Tsigaridis & Kanakidou, 2018) and impacting SOA. Aerosol hydration in OMA is calculated in the radiation code following (Tang & Munkelwitz, 1994). Sea salt has two distinct size classes, and dust is described by a sectional model with an option of choosing from 4 to 6 bins. The default dust configuration, used here, includes 5 bins, a clay and 4 silt classes, from submicron to 16 μm in radius. Like MATRIX, OMA includes only the first indirect effect. The aerosol number concentrations that impact clouds are obtained from the aerosol mass as described in Menon and Rotstayn (2006). All aerosol species can activate clouds, including dust in case it is coated with inorganic coatings.

The interactive composition runs, either using MATRIX or OMA, include aerosol-cloud effects, but only affecting cloud optical depth, in stratiform and convective clouds, not interfering with cloud microphysics. As such only considered the first indirect, the Twomey effect (Twomey, 1977) and intrinsically via radiation feedbacks semi-direct effects. The newly release NASA GISS ModelE3.1 (GISS-E3) (Cesana et al., 2019, 2021) includes a two-moment stratiform cloud microphysical scheme now considers the Twomey as well as effects associated with microphysically induced changes and precipitation, however this version was not used here. Note that ice cloud physics are only impacted via indirect pathways by aerosols. Direct ice nucleation pathways are not included in this model version.

The treatment of prescribed (anthropogenic and biomass burning) emissions is identical for both aerosol models. Sea salt, DMS, isoprene and dust emission fluxes are calculated interactively. The remaining anthropogenic fluxes come from the Community Emissions Data System (CEDS) inventory (Hoesly et al., 2018). Biomass burning comes from either the GFED4s inventory (van der Werf et al., 2017) for the 1997–2014 period or from (van Marle et al., 2017) before 1997. The future scenario emissions are based on (Feng et al., 2020; Gidden et al., 2019; Meinshausen et al., 2020; O'Neill et al., 2016). We analyze the four CMIP6 Tier 1 Shared Socioeconomic Pathways (SSPs): a sustainable scenario on the low end of the range SSP1-2.6, a medium range SSP2-4.5, a regional rivalry scenario in the medium to high end of the range SSP3-7.0, and a fossil-fueled development high end of the range of future pathways SSP 5–8.5. All other forcings, such as solar, volcanic (prescribed as stratospheric AOD and aerosol size) and land-use follow the CMIP6 protocol (Eyring et al., 2016).

The spin-up of the historical simulations is described in Miller et al. (2021). The future scenario simulations (2015–2100) are started from the end point of the historical coupled simulations and are discussed in a future publication. All results shown are averaged over the ensemble members.

GHG and aerosol forcings are calculated using multiple calls to the radiation model. GHG forcings are calculated following the CMIP protocol against pre-industrial conditions using the following mixing rations per GHG: CO_2 284.317 ppm, N_2O 0.273 ppm, CH_4, 0.808 ppm, CFC-11 and CFC-12, 0.0 ppm. Aerosol forcings are calculated using two radiation calls every fifth model timestep, one with and one without aerosols. Aerosol indirect forcing (ACI) calculations follow the definition by Ghan (2013), using the difference in cloud radiative forcing calculated as a diagnostic with aerosol scattering and absorption omitted under all sky and clear sky conditions. This requires four additional calls to the radiation. Eruptive volcanic emissions are not included in the ACI and ARI calculations, as volcanic AOD is used to represent volcanoes in this model version. All forcing numbers reported here are instantaneous. The difference between instantaneous and effective aerosol forcings for the GISS CMIP6 model are reported in Bauer et al. (2020) and Miller et al. (2021).

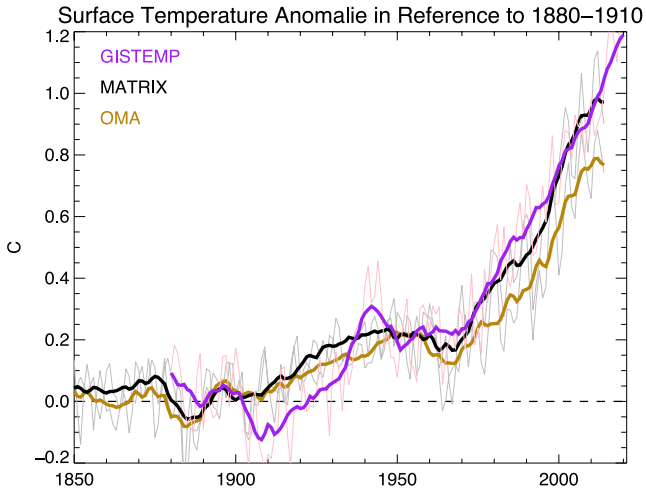

Figure 2. Ensemble, global, and annual-average surface air temperature anomalie (°C), in reference to 1880–1910, during the historical simulations (1850–2014). MATRIX in black and OMA in brown and observational data GISTEMP (1880–2020) in purple. Thin lines show annual data, thick lines show temporal smoothed data using a 10-year running filter.

The digital object identifier (DOI) for each simulation is listed in Table S1 of Supporting Information S1. The OMA version is designated as physics-version p3 and MATRIX is designated as physics-version p5 in the CMIP6 archive.

2.2. Single Forcing Runs

The single forcing runs are carried out with the OMA model. All forcings are set to 1850 conditions, except the single forcing that is allowed to change over time. The forcings applied here are volcanoes, land surface changes (not impacting GHG levels), solar, and aerosols (including all non-volcanic sources). The single forcing runs for long-lived greenhouse gases (GHGs), including carbon dioxide, methane, nitrous oxide and chlorofluorocarbons (CFCs) uses the non-interactive NINT model version, physic-version1 (p1). More details on the NINT setup can be found in Kelley et al. (2020) and Miller et al. (2021). The NINT model does not calculate interactive atmospheric composition, but instead reads in ozone and aerosol fields from an OMA simulation with observed SST (Bauer et al., 2020). Five ensemble runs are carried out for each single forcing.

3. Results

In this study, we present results from the ocean-atmosphere-composition climate simulations. Surface air temperature for the historical ensembles is plotted in Figure 2 along with the GISTEMP Land-Ocean Temperature Index (LOTI) (Lenssen et al., 2019). The GISTEMP LOTI includes SST and land surface air temperature data (http://data.giss.nasa.gov/gistemp/). Anomalies are defined in reference to 1880 to 1910. Similar to CMIP5 models (Miller et al., 2014, 2021), the models here still run warm at the beginning of the 20th century (Figure 2), an occurrence known as the Early Twentieth Century Warming (ETCW). Hegerl et al. (2018) attributed about half of the global warming between 1901 and 1950 to a combination of increasing greenhouse gases and natural forcing, offset to some extent by aerosols. Natural variability also made a large contribution to warming, particularly to regional anomalies like the Arctic warming in the 1920s and 1930s (Hegerl et al., 2018). The ETCW period also encompassed exceptional events, such as the Indian monsoon failures around the turn of the twentieth century, the "Dust Bowl" droughts and extreme heat waves in North America in the 1930s, drought in Australia between 1937 and 1945; and the European droughts and heat waves of the late 1940s and early 1950s. Some of the deviations between LOTI observations and models during ETCW are due to internal variability and are within the uncertainty of the observed global average (about 0.1°C at the 95% level) during this period (Lenssen et al., 2019). In addition, natural and anthropogenic forcings during that period are uncertain as well.

After the ETCW, the MATRIX simulation matches the observational data well (Figure 2); the OMA model is biased too cold. By 2014, GISTEMP records warming (relative to 1950–1980) of 0.75°C, compared to warming within MATRIX and OMA of 0.74°C and OMA 0.60°C, respectively. MATRIX total aerosol forcing is weaker than in OMA, consistent with a better match in surface temperature. Contrasting 10-year means for 1850–1859 and 2005–2014, net aerosol forcing equals -1.36 Wm^{-2} (-0.28 (RFari), -1.08 (RFaci)) for MATRIX and -1.85 Wm^{-2} (-0.31 RFari, -1.54 RFaci) for OMA (Bauer et al., 2020).

The IPCC AR6 (Forster et al., 2021) reports an observationally based instantaneous RFari of -0.4 ± 0.4 W m^{-2} and the corresponding model-based assessment of -0.2 ± 0.2 Wm^{-2}. By combining these assessments, the report estimates RFari to be -0.25 ± 0.2 W m–2 (*medium confidence*).

In contrast, the IPCC assessment of the effective RFaci based on observational evidence alone (-1.0 ± 0.7 W m^{-2}) is almost identical to the one based on model evidence (-1.0 ± 0.8 W m^{-2}) with an overall assessment of the central estimate and *very likely* range for effective RFaci of -1.0 ± 0.7 W m^{-2} (*medium confidence*).

Compared to CMIP6, the weaker RFaci of the MATRIX model, compared to OMA, is a better match to the observed and model assessments in the AR6, and corresponds to a better match by MATRIX to the observed

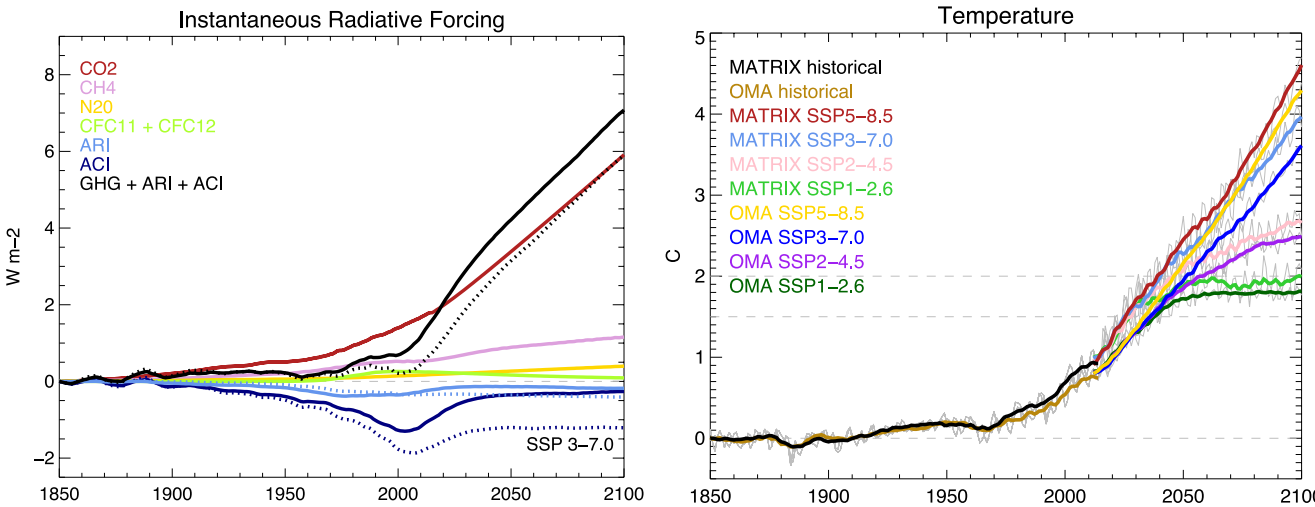

Figure 3. Top of the atmosphere instantaneous radiative forcing (left) and global mean surface temperature (right) anomalies, in reference to 1850–1859. The sum of GHG and aerosol forcing (black) is shown and its contributions from the GHGs, CO_2 (red), methane (pink), nitrous oxide (yellow), and CFCs (green), as well as the forcing from aerosol-radiation interactions (ARI, light blue) and aerosol-cloud interactions (ACI, dark blue). The historical period, as simulated by MATRIX (solid lines) and OMA (dotted lines), until 2014, is followed by SSP 3–7.0 simulations in the left plot. The temperature plot (right) shows time series for the MATRIX (black) and OMA (brown), and for SSP1-2.6, 2–4.5, 3–7.0, and 5–8.5. The thin gray lines show annual data, and the thick colored lines temporally smoothed data, using a 10-year moving average.

temperature trend (Figure 2). Matching the observed temperature does not prove that the model aerosol forcing is correct, as other processes such as ocean heat uptake play important roles in determining the rate of warming. However, agreement of the MATRIX forcing with the IPCC estimate suggests that the model aerosols are making the right contribution to the temperature trend. More details about the GISS model's historical climate simulations are given in Miller et al. (2021) and Bauer et al. (2020).

3.1. Global Forcings

Global warming is the response of the climate system to forcings. By 2014, the main forcing agents (Figure 3, left) are the greenhouse gases (GHG) carbon dioxide (CO_2: 1.79 Wm^{-2}), methane (CH_4: 0.55 Wm^{-2}), nitrous oxide (N_2O: 0.18 Wm^{-2}) and chlorofluorocarbons (CFCs: 0.24 Wm^{-2}), the forcing caused by aerosol-radiation interactions (RFari: −0.28 Wm^{-2}) and aerosol-cloud interactions (RFaci: −1.08 Wm^{-2}). The numbers in brackets show the difference in top of the atmosphere (TOA) radiative forcing between 1850 and 2014, using the MATRIX aerosol module. In addition, the climate system, and ModelE, is driven by forcing caused by changes in tropospheric and stratospheric ozone, land-use, irrigation, volcanic eruptions (prescribed as stratospheric AOD), surface albedo, orbital and solar radiation cycles, as discussed in Miller et al. (2021).

Figure 3 (left) includes the continuation of the historical simulation using the future scenario SSP3-7.0. Figure S1 in Supporting Information S1 shows in addition scenarios, SSP1-2.6, 2–4.5, and 5–8.5. The resulting global surface temperature (Figure 3, right) anomalies show that Earth will warm between 2 and 5°C by the end of the century in reference to 1850, depending on the scenario chosen. For all simulations, the MATRIX model shows a stronger warming, which is caused by an overall smaller RFaci compared to OMA. Note that even in SSP1-2.6, the most optimistic scenario, the ModelE climate warms beyond 1.5°C globally. All other scenarios, SSP 2–4.5, SSP 3–7.0, and SSP 5–8.5, warming exceeds 2°C global warming.

Table 1 and Figure 4 shows that the turning point in RFari does depend on the individual aerosol module used, MATRIX or OMA, and the SSP. However, for all but two cases, SSP3-7.0 and SSP5-8.5 OMA, RFari has reached its turning point in the historical period. The turning point date for RFaci only depends on the model, as it always falls within the historical period. The fact that in all cases, the global magnitude of RFari is smaller than RFaci (Figure 4) by a factor of four in MATRIX, and five in OMA, leads to the conclusion that the turning point of maximal aerosol forcing has already passed. The following sections will explain the details behind these findings.

Table 1
Year of the Maximal Aerosol Forcing Effect, Using a Rolling 10-Year Average Filter

	SSP1-2.6		SSP2-4.5		SSP3-7.0		SSP5-8.5	
SSP after historical	MATRIX	OMA	MATRIX	OMA	MATRIX	OMA	MATRIX	OMA
RFari	1977(±1)	2009(±3)	1977(±1)	2009(±3)	1977(±1)	2100(±2)	1977(±1)	2066(±4)
RFaci	2003(±1)	2007(±2)	2003(±1)	2007(±2)	2003(±1)	2007(±2)	2003(±1)	2007(±2)
RFari + RFaci	2001(±3)	2007(±2)	2001(±3)	2007(±2)	2001(±3)	2007(±2)	2001(±3)	2007(±2)

Note. Uncertainty, given in brackets, calculated using filters varying between 1 and 10-year averages.

3.2. Radiative Forcing From Aerosol-Radiation Interactions (RFari)

The aerosol composition simulation including a trend analysis of the historical period of ModelE using MATRIX and OMA has been discussed and evaluated against observations, including satellite AOD and radiation fluxes, mass concentrations from surface networks and ice cores (Bauer et al., 2020). The only difference in setup between the evaluated runs and the runs here are that (Bauer et al., 2020) used an AMIP ensemble, with prescribed sea surface temperature and sea ice extent and thickness, while this paper uses a coupled ocean configuration. The composition of gases and aerosols simulated with a dynamical ocean is very similar compared to that of the previously evaluated AMIP simulations. Bauer et al. (2020) showed that observations often fall between the two aerosol modules when comparing satellite aerosol optical depth (AOD) and Clouds and Radiation Energy Systems (CERES) clear-sky TOA radiative fluxes. Overall, MATRIX simulates larger burdens of sulfate aerosols compared to OMA, which agree better with surface observations in Europe and the Eastern US, while OMA simulates larger burdens of organic aerosol compared to MATRIX, which compares better to observations in the US. For more details on the aerosol evaluation and trend analysis please refer to Bauer et al. (2020).

The evolution of total atmospheric aerosol load from the historical period to 2100 is shown in Figure 5. The breakdown of the global-mean time series into regional ones, as defined in Figure S2 of Supporting Information S1, is presented in Figures S3–S6 of Supporting Information S1 for sulfate, organic aerosol, BC and nitrate. The two aerosol modules are mostly consistent during both the historical period and the future scenarios in their relative aerosol masses: MATRIX simulates higher sulfate and sea-salt loads with higher loads of organic aerosol, nitrate, black carbon and dust in OMA. The trends are very consistent among all simulations, as they are driven by the same anthropogenic and biomass burning emission inventories. Sulfate mass is larger in MATRIX, compared to OMA, because of microphysical processes, including new particle formation by nucleation as well as different lifetime effects, due to the presence of sulfates over all aerosol size classes. The larger aboundance of sulfate in MATRIX leads to smaller amounts of nitrate due to the competition for ammonium between sulfate and nitrate. OA differs between the models, because OMA includes a more detailed calculation of secondary organic aerosols

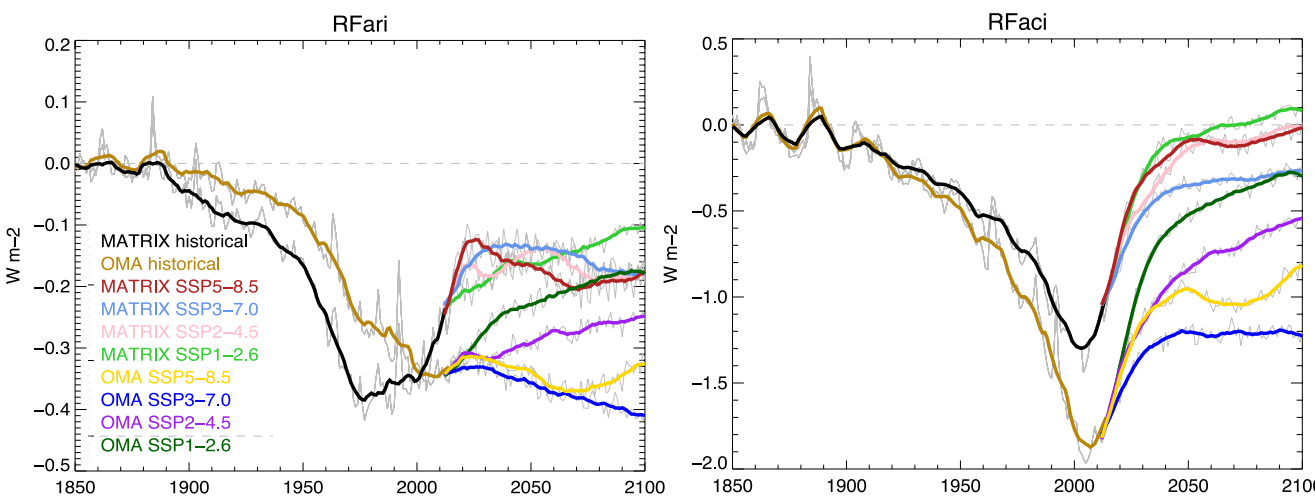

Figure 4. Instantaneous aerosol radiative forcings, in reference to 1850–1859, RFari (left) and RFaci (right).

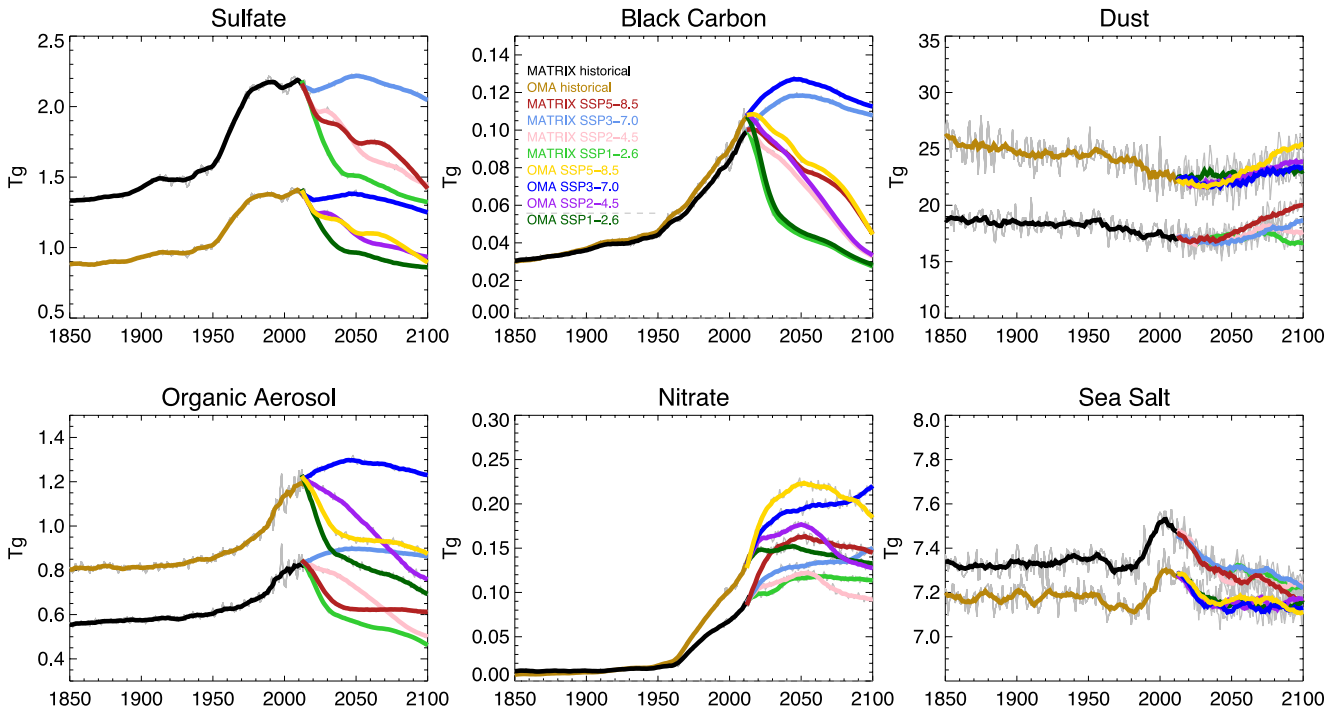

Figure 5. Time series of globally averaged loads (Tg) of sulfate, black carbon, dust, organic aerosol, nitrate and sea salt. Legend as in Figure 4.

(SOA) compared to MATRIX. MATRIX considers SOA production as a yield that possibly underestimates the overall contribution of SOA to OA. However, this statement is based on measurements over the US, as global evaluation of SOA and OA remains challenging (Tsigaridis et al., 2014). The large year-to-year variability (gray lines in Figure 4 and Figures S4 and S5 in Supporting Information S1) in OA and BC between 1997 and 2014 is caused by the use of satellite-derived biomass burning emissions during that period. Black carbon concentrations are very similar between the aerosol schemes, especially since the lifetime of BC was tuned in OMA to match that of MATRIX (Bauer, Bausch, et al., 2013). The overall load of sea salt and dust differs between the modules, as different size distributions are represented, but the trends are similar. OMA includes 5 bins for dust aerosol and two bins for sea salt (Miller et al., 2006). MATRIX dust and sea salt are emitted into two modal size distributions, respectively, but can evolve due to microphysical processes (Bauer et al., 2008). Overall, due to the differences in dust particle size between the MATRIX modes and OMA bins, MATRIX does not fully represent coarse dust above 5 μm diameter, and as such has an overall smaller dust load, compared to OMA. This bias should not translate into a large bias in forcing, where coarse dust particles only have small albeit positive impacts (Adebiyi & Kok, 2020; Kok et al., 2017). In both aerosol modules, dust lifetime depends on coatings of water soluble materials: in OMA due to heterogeneous chemistry on dust surfaces (Bauer & Koch, 2005) and in MATRIX due to the internal mixing of aerosols (Bauer et al., 2008). As such, under changing pollution levels, dust wet removal rates can change over time. During the historical period, the main driver behind trends in dust is the impact of irrigation on dust emissions. Increased irrigation especially since 1950 until present has lead to deceasing dust emissions, translating directly into a lower global dust load (Figure 5). The future scenarios show increases in dust again, that we speculate might be linked to changing rainfall patterns. Anthropogenic dust, such as agricultural or road dust are not part of the models parameterization, only desert dust sources are included in the model. Inclusion of more anthropogenic dust sources can have impacts on future dust forcings, certainly an area that needs further research. Trends in sea salt are caused by changes in wind patterns, especially over the Southern Oceans. We expect a similar climate-induced change in sea salt number emissions as discussed in Struthers et al. (2013), where trends in the Southern Ocean explain the strong variability in sea salt affecting the global trend.

After discussing the global composition trends by aerosol species, the next step is to explain the trends in forcing. Due to the extra computational costs that multiple radiation calls add to the overall run time of the simulations, we only have the individual forcing numbers by aerosol species available for a pre-industrial and present-day simulation (Table 2). This single aerosol species forcing computation can only be carried out with the OMA

Table 2
Pre-Industrial (1850–1859) to Present Day (2005–2014) $RF_s ari$ (W/m^2) at the Top of the Atmosphere Radiative Forcing for OMA

	$RF_s ari$ (sum over species)	Sulfate	OA	BC	Nitrate	Dust	Sea-salt
SW	−0.22	−0.31	−0.07	0.22	−0.16	0.10	0.01
LW	−0.03	0.01	0.00	0.00	0.01	−0.05	−0.00
Net	−0.25	−0.31	−0.07	0.22	−0.15	0.05	0.01

Note. The total forcing $RF_s ari$, is the sum over the six aerosol components in this table, and differ from RFari (−0.28 W/m^2), due to nonlinearities in forcing calculations using individual species versus all aerosols.

model, as MATRIX carries internally mixed aerosols. MATRIX single component forcing calculations would only give insight into forcing by MATRIX uniquely defined aerosol populations and not the traditional chemical species. This information is too model specific to be useful to report.

RFari is controlled by all aerosol species, except sea-salt, whose forcing trend is too small to matter. Dust forcing, in accordance with a negative trend in load between pre-industrial and present day is positive. This forcing has its strongest impact in Northern Hemispheric Africa, followed by the Middle East.

On a global basis (Figure 4 and Table 1), MATRIX shows the largest RFari in 1977(±1), coincident with the peak in SO_2 emissions in the United States, Europe and Western Central Asia. Because this time falls into the historical period, the individual SSP simulations don't change this result. The OMA RFari peak, because of the smaller sulfate effect in that module, depends on the individual SSP. For SSP1-2.6 and SSP2-4.5 the maximal RFari falls into the historical period, the year 2007(±2), in accordance with peak concentrations of organic aerosol, nitrate and sulfate in Central and South East Asia. In SSP3-7.0 nitrate and OA aerosol forcing is projected to gives its largest forcing by the end of the 21st century. In scenarios SSP5-8.5 and SSP3-7.0, OMAs maximal RFari is reached by 2066(±4), and the end of the 21st century, respectively.

SSP1-2.6, the lowest GHG scenario, also has the lowest overall aerosol and aerosol precursor emissions. Under that scenario, sulfate (Figure S3 in Supporting Information S1) reaches preindustrial levels in all regions of the world by the end of the century and shows steady declines between today and 2100. Carbonaceous aerosols, OA and BC show very similar regional trends (Figures S4 and S5 in Supporting Information S1), as they share sources such as biomass burning, residential and commercial emissions, but lead to opposite forcings. BC positive forcing dominates over OA negative forcing (Table 2). In SSP1-2.6 carbonaceous aerosols decline even below pre-industrial values, due to the presence of deforestation and biomass burning during pre-industrial times. This is also visible in Figure 6 and Figure S7 in Supporting Information S1, showing that highest OA concentrations over Europe and Eastern US were already reached at the beginning of the simulation. The only increasing aerosol trend is seen in nitrate aerosols in some parts of the world, such as the Middle East and Africa, due to increased ammonia emissions associated with food production (Bauer et al., 2016).

SSP2-4.5 includes larger aerosol and aerosol precursor emissions than SSP1-2.6, but still reflects globally decreasing emissions until the end of the century. Most notably is the later occurrence of maximal emissions in Asia, compared to SSP1-2.6, which projects an immediate downturn of emissions, while SSP2-4.5 emission peaks around the year 2030 in Asia. Still, in this scenario, OMA and MATRIX show maximal global RFari during the historical period.

SSP3-7.0, projects the largest aerosol precursor emissions, even though it has lower GHG concentrations than SSP5-8.5. Some regions of the world have increasing trends, compared to present day, in SO_2 and carbonaceous aerosol, like South and Central America, and Africa, and maximum emissions in the Middle East and Asia around the year 2050. Ammonia emissions are continuously increasing in Southeast Asia. For this scenario, Figure 6 shows maps of the timing of maximal concentrations or forcings, respectively, for the MATRIX model. Sulfate has a clear pattern of shifting from maximum concentrations in 1970–1980 in the middle and high latitudes toward the tropical regions. The earliest sulfate peak appeared in the USA, followed by Europe. North and Eastern China had its largest sulfate concentrations in the last decade. Southeast Asian and Indian largest values are found in 2050 and later. Organic aerosol concentrations show a more limited and later reduction in high latitudes, compared to sulfate, and some very early (before 1950) maximal concentrations caused by deforestation in Europe and the Eastern US. Organic aerosol in China has not yet reached its maximum concentrations. The sources of organic aerosol are strongly linked to biomass burning, and as such differ from patterns of other anthropogenic and more technology-related emissions.

Regional trends in MATRIX AOD (Figure 6 and Figure S7 in Supporting Information S1) mostly follow the pattern of sulfate mass and as such overall explain the regional and global RFari trends (Figure 4). The timing map of RFari in MATRIX shows that most of the world has already experienced the largest aerosol direct effect, except India, Southeast Asia and NH South America. However, emissions from those regions are rather small

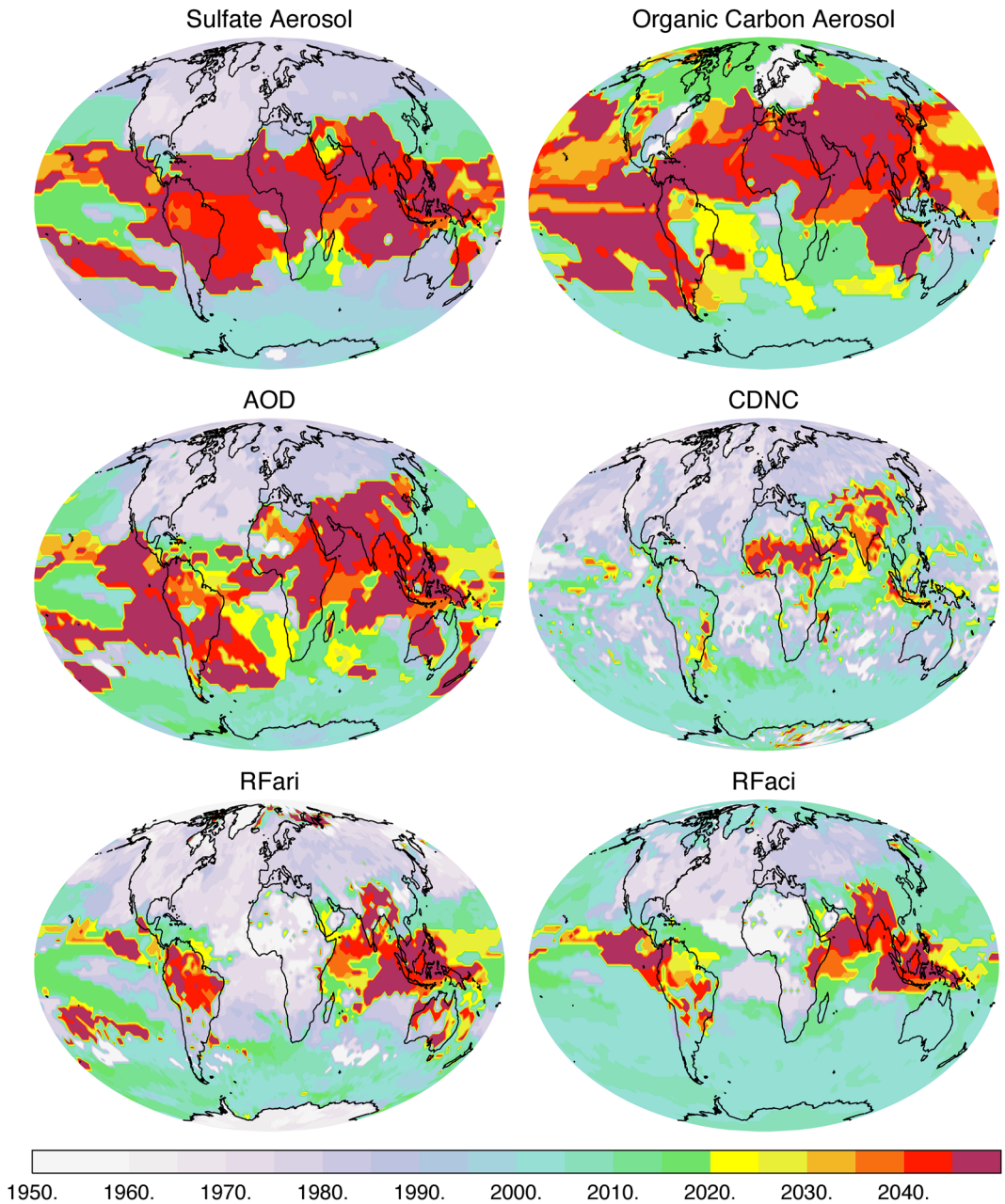

Figure 6. Maps of the year, between 1950 and 2050, when the displayed quantity reached its maximal annual value. Results are shown for the MATRIX historical and SSP 3–7.0 simulation. The same maps for OMA are shown in Figure S5 of Supporting Information S1.

compared to the rest of the world. The main difference between OMA (Figure S7 in Supporting Information S1) and MATRIX, is that the maximal timing of RFari expands over a wider area in Asia in OMA, caused by the smaller presence of sulfate in that module.

MATRIX shows maximal global forcing RFari under SSP3-7.0 for the same year as in all other scenarios, 1977(±1) (Table 1), still driven by the strong sulfate forcing in the USA and Europe during those times, whereas OMA pushes its maximum toward the end of the simulation, reacting more to the strong Asian and African forcings linked to organic aerosols.

SSP5-8.5, the scenario with the largest GHG concentrations and strongest forcings, places its aerosol and gas precursor emissions somewhere between SSP3-7.0 and SSP2-4.5. As a result, the MATRIX RFari peak forcing

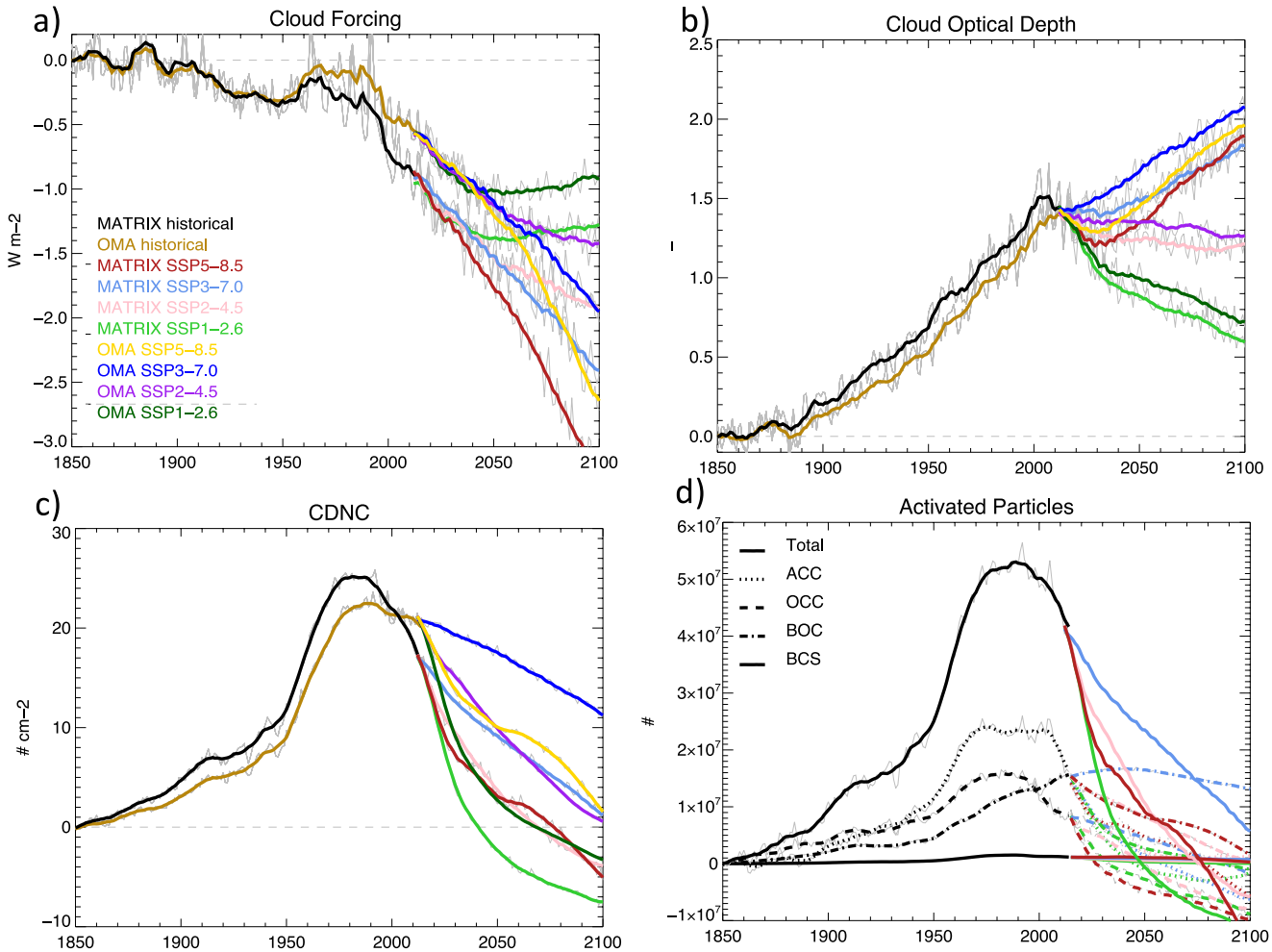

Figure 7. Time series of global mean anomalies, in cloud forcing (top left), cloud optical thickness (top right) and cloud droplet number concentrations (lower left). Activated aerosol number concentrations for MATRIX (lower right). Displayed are number concentrations, in # averaged over 0–3,000 m, depending on aerosol mixing state: ACC (predominantly sulfate and nitrate), OCC (mainly organic aerosol), BOC (mainly carbonaceous mixtures), BCS (mainly sulfate with black carbon mixtures).

agrees with its timing in all the other scenarios, in 1977, while the OMA RFari peaks in 2066(±4), in between what was seen in SSP3-7.0 and SSP2-4.5.

3.3. Radiative Forcing From Aerosol-Cloud Interactions (RFaci)

The global aerosol forcing is dominated by aerosol-cloud interactions. RFaci is about four times larger in magnitude than RFari in MATRIX and five times in OMA. Thus, understanding trends in RFaci is key in identifying trends in aerosol forcing.

The climate model shows two different trends in terms of cloud effects, first RFaci, which is caused by aerosols and second the overall cloud change, which is caused by global warming and as such is a feedback. The radiative effect of changing clouds (Figure 7, top left) is calculated as the difference between the radiative energy budget of clear-sky and all-sky conditions. In general cloud trends are linked to trends in specific humidity (Figure S7 in Supporting Information S1), which is driven by temperature and the fact that a warmer atmosphere can hold more water. The main known features (Ceppi et al., 2017) (a) rising free-tropospheric clouds (a positive longwave effect); (b) decreasing tropical low cloud amount (a positive shortwave effect); (c) increasing high-latitude low cloud optical depth (a negative shortwave effect), explain the cloud radiative forcing trends. Rising high clouds are consistent with the fixed anvil temperature hypothesis. Tropical low cloud amount decreases are driven by

a delicate balance between the effects of vertical turbulent fluxes, radiative cooling, large-scale subsidence, and lower-tropospheric stability on the boundary-layer moisture budget (Ceppi et al., 2017).

In order to untangle the aerosol-cloud forcing RFaci, it should be mentioned that the two aerosol modules differ in how aerosols translate into CDNCs, as explained in the model description. Cloud droplet number concentrations (CDNC) show future maximum values (Figure 6) only in parts of Asia, equatorial Africa and South America, explaining the resulting indirect effects RFaci in those regions. Note that equatorial Africa, which is dominated by convective cloud systems, is not very susceptible to the CDNC changes there. The global mean trends in CDNC (Figure 7c) maximize within the historical period, despite the fact that SSP3-7.0 has increasing aerosol emissions.

In MATRIX we can further look into the chemical composition of the activated aerosol particles (Figure 7d), this analysis is not possible for OMA, as the CCN diagnostics are not included. The trend in CDNC is similar to the trend in activated aerosol species (Figure 7d). The main contributions to the trend in activated aerosols, and thus CDNC, are sulfate/nitrate/NH_4 aerosols (ACC), organic aerosol (OCC), and mixtures or carbonaceous aerosol (BOC) and to a small extent BCS, which are black carbon-sulfate/nitrate/NH_4 mixed particles. The other internally mixed aerosol populations in MATRIX, explained in detail in (Bauer, Ault, & Prather, 2013; Bauer et al., 2008), do not present any noticeable trend in activation. Some other aerosol types, like fine sea salt and mixing states including sulfate from oceanic DMS production, contribute significantly to the total amount of CDNC as well, but they do not contribute to the trend as their variations with time are much smaller compared to trends driven by SO_2, carbonaceous emissions and nitrate precursors.

The global evolution of cloud optical thickness in MATRIX (Figure 7b) differs from that of CDNC. The peak in cloud optical thickness during the historical simulations coincides with the peak in RFaci in MATRIX. However, in the future scenario simulations, global cloud optical thickness either increases or decreases, depending on the SSP, and most likely is driven more by climate than by aerosol changes. More research is needed to detangle aerosol from climate change effects on future cloud trends.

In order to understand why RFaci reaches its largest forcings one or two decades after global peak concentrations in CDNC, which coincides with aerosol mass trends, we look at their regional behaviors. Figure 8 shows the global and regional normalized absolute changes (regional means divided by global time averaged means) in CDNC and RFaci, for the regions (as defined in Figure S2 of Supporting Information S1) experiencing the largest aerosol-cloud interaction effects. Regionally, the temporal evolution of CDNC and RFaci are highly correlated. The global maximum, or turning point of RFaci from increasing to decreasing, falls in between the strong aerosol-cloud effects happening in the US, Europe and Western Central Asia around the 1980s, and their later peak in Eastern Central and Southeast Asia. The temporal shift between global trends in CDNC (peaking in 1990) and RFaci (early 2000) is explained by the overall much stronger RFaci in Asia, compared Europe and the US, as can be seen in the normalized plots in Figure 8. Eastern and Southeastern Asia, areas that experience high aerosol loads, have a strong global impact on the timing of the overall aerosol-cloud forcing.

MATRIX and OMA RFaci differ most strongly in Eastern Central and Southeastern Asia in the future projection (Figure 6; Figures S5 and S8 in Supporting Information S1). These differences follow closely the simulated OA in the two regions (Figure S4 in Supporting Information S1), and is mostly attributed to the difference in OA caused by the simplified (MATRIX) versus explicit treatment (OMA) of secondary organic aerosol formation (see Section 2). The increased SOA from isoprene (reacting to a warmer climate) in the future in OMA is expected to affect this difference, since more isoprene SOA sources will increase overall OA (Tsigaridis & Kanakidou, 2018). However, this does not change the global turning point of RFaci, but is important in order to understand future aerosol-cloud effects, involving biogenic organics.

3.4. Counterbalance Between GHG and Aerosol Forcing

Looking at the balance between aerosol and GHG forcings (Figure 9), it is obvious that the ability of aerosols to counterbalance greenhouse gases has strongly been diminished in recent decades. While between 1960 and 1980 aerosols where able to counterbalance up to 80% of the total GHG forcing, there has been a strong decrease in this compensation since then. At present (as indicated by the vertical line in Figure 9), aerosol forcing in MATRIX only counterbalances about 20% of GHG forcing. There has been a dramatic shift between the strength in GHG and aerosol forcings over the past 20 years. As a consequence, limiting aerosol concentrations and their

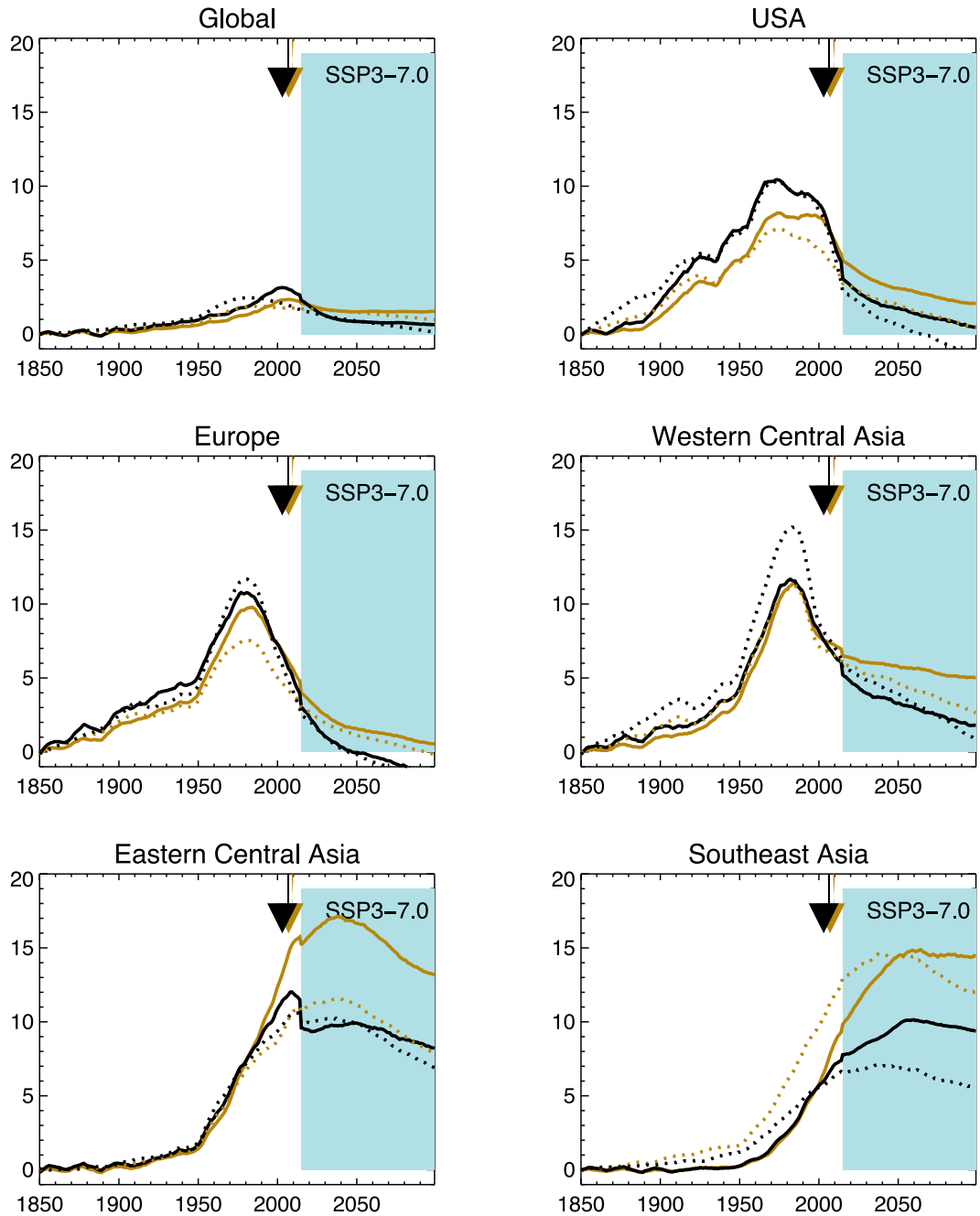

Figure 8. Time series of globally normalized absolute changes in RFaci (solid lines) and CDNC (dashed) changes since 1850–1860. The global and regional RFaci and CDNC values are normalized (to 1.) against their global mean, averaged between 1850 and 2100. The historical and SSP3-7.0 simulation (blue shaded area) is shown for MATRIX (black) and OMA (brown). The arrows indicate the year of maximal global RFaci. The regions are shown that contribute most to RFaci. Regions as defined in Figure S2 of Supporting Information S1.

net global cooling effect is accelerating present and future global warming. By the end of this century, aerosols will only counterbalance 0%–20% of GHG forcings, depending on the aerosol model and future scenario. In 2100 the robustness of this result depends more on the individual aerosol scheme than on the SSP. The difference between SSPs is of the order of less than 10%, while the aerosol modules show larger differences between them. Considering the dominating impact of aerosol-cloud interactions, it is of great interest to extend this analysis to other climate models.

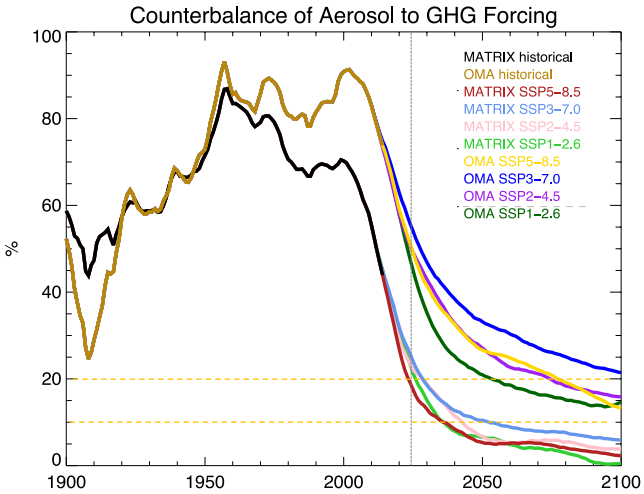

Figure 9. Relationship between GHG, including CO_2, CH_4, N_2O, CFCs, and absolute net aerosol forcings. Percentage changes before 1900 are omitted because the individual forcings were too small to give meaningful percentage changes. Horizontal and vertical lines highlight the year 2022, and 10 as well as 20% levels.

4. Conclusion

Trends in aerosol are diverse, depending on source and geographical region. While many regions in the Northern Hemisphere have seen decreasing emissions for decades, reduction in Asia have been more recent, with some countries such as China having recently reversed their trends by decreasing emissions, while other regions, such as India or parts of South Asia, are still on an increasing trajectory. Based on the results of the GISS-E2.1-G coupled model, the total aerosol forcing has reached its turning point, switching from globally increasing to decreasing in the first decade of the 21st century. This conclusion is based additionally upon the CEDS CMIP6 and scenario emission inventories, although there is no guarantee that any SSP captures the actual future emission pathway. The IPCC AR6 (Forster et al., 2021) agrees with our finding in terms of the trend in global mean RFari: direct aerosol forcing reached its maximum negative value in the mid-1970s and its magnitude gradually decreased thereafter. This weakening of the negative forcing since 1990 has been attributed to a reduction in global mean SO_2 emissions combined with an increase in global BC (Myhre et al., 2017).

Observational analyses based on satellite products (Quaas et al., 2022) concur with our results: the regions in which aerosol emissions declined (in particular North America, Europe and East Asia) dominate over regions with increasing trends. The overall climate-relevant signal is a decline in negative aerosol effective radiative forcing by about 0.1–0.3 W/m^2 (Quaas et al., 2022).

The model, under its current configuration, closely simulates the observed historical surface temperature, especially MATRIX (Miller et al., 2021), and is in the mid-range of climate sensitivity estimates (ECS) compared to other models (Zelinka et al., 2020), indicating that the historical trend in aerosol-cloud induced forcings is reasonable in magnitude. OMA's effective ECS is 2.6°C and MATRIX is 2.8°C. The IPCC AR6 report (Forster et al., 2021) best estimate of ECS is 3°C with the *likely* range of 2.5–4°C and the *very likely* range of 2–5°C. Hausfather et al. (2022) that discusses the hot model problem in CMIP6 confirms the "likely" 2.5–4°C ECS of the IPCC AR6 report (Forster et al., 2021).

The emission inventories, especially the future scenarios, are by their nature highly speculative. However, the fact that our conclusion of peak aerosol timing is independent of what scenario we follow, including a scenario with strongly increasing future aerosol trends, SSP3-7.0, does provide confidence in the results.

The model shows that spatial and temporal distributions of aerosol direct forcing are directly linked to the overall load of aerosol mass in the atmosphere. Much of the global forcing trends are dominated by trends in sulfate. Sulfate is only expected to increase in very few, currently low-to-medium income countries in the world, but not globally. The fact that anthropogenic SO_2 emissions are decreasing in China (Ramachandran et al., 2020) further decreases the impacts of aerosols on global climate. Technologies like sulfur dioxide scrubbers and international regulations, for example, the International Convention for the Prevention of Pollution from Ships (www.imo.org), will lead to further decreases in SO_2 emissions. Global trends in organic and BC aerosol, in addition to natural and industrial sources, also depend on biomass burning, which accounts for one-third of global organic aerosol emissions at present. Historical biomass estimates can greatly impact forcing (Liu et al., 2021) and future biomass burning is highly speculative. This topic certainly needs attention in future studies. Ammonium-Nitrate aerosol is very likely to keep increasing into the future, due to its strong link to food production. However, the radiative forcing of nitrate aerosol is not well understood, and models disagree in its magnitude, pointing to the need for further studies as well as more measurements. Aerosol-cloud induced forcings on the other hand do not simply follow trends in aerosol or AOD loads. ACI are much more non-linear, with stronger dependencies on regions and cloud regimes. This points to the importance of studying ACI under future climate conditions, using models with detailed aerosol-cloud microphysical parameterizations. Equally important will be an improved understanding of trends in natural and other terrestrial emissions in a warmer and less polluted climate. Nonetheless, the future

climate of our planet as simulated by the GISS model is marked by decreasing aerosol forcings and evermore dominating GHG effects.

Data Availability Statement

All model simulations are available at the CMIP6 data portals: USA, PCMDI/LLNL (California)—https://esgf-node.llnl.gov/projects/cmip6/, France, IPSL—https://esgf-node.ipsl.upmc.fr/projects/cmip6-ipsl/, Germany, DKRZ—https://esgf-data.dkrz.de/projects/cmip6-dkrz/ or UK, CEDA—https://esgf-index1.ceda.ac.uk/projects/cmip6-ceda/. In addition, the GISS simulations are available at our local data share point: https://portal.nccs.nasa.gov/datashare/giss_cmip6/. The GISTEMP data are available from https://data.giss.nasa.gov/gistemp. Processed data of the ensemble mean global and regional time series of the GISS model runs as used in this paper are available at: (Bauer et al., 2022, https://portal.nccs.nasa.gov/datashare/GISS/ModelE_tracers/papers/Bauer_et_al_2022/).

Acknowledgments
Resources supporting this work were provided by the NASA High-End Computing (HEC) Program through the NASA Center for Climate Simulation (NCCS) at Goddard Space Flight Center. The model simulations are available at the CMIP6 data portals. All authors acknowledge funding from the NASA Modeling and Analysis program.

References

Abdul-Razzak, H., & Ghan, S. J. (2000). A parameterization of aerosol activation: 2. Multiple aerosol types. *Journal of Geophysical Research*, *105*(D5), 6837–6844. https://doi.org/10.1029/1999JD901161

Abdul-Razzak, H., Ghan, S. J., & Rivera-Carpio, C. (1998). A parameterization of aerosol activation: 1. Single aerosol type. *Journal of Geophysical Research*, *103*(D6), 6123–6131. https://doi.org/10.1029/97JD03735

Adebiyi, A. A., & Kok, J. F. (2020). Climate models miss most of the coarse dust in the atmosphere. *Science Advances*, *6*(15), eaaz9507. https://doi.org/10.1126/sciadv.aaz9507

Arias, P. A., Bellouin, N., Coppola, E., Jones, R. G., Krinner, G., Marotzke, J., et al. (2021). Technical summary. In V. Masson-Delmotte, P. Zhai, A. Pirani, S. L. Connors, C. Péan, S. Berger, et al. (Eds.), *Climate Change 2021: The Physical Science Basis. Contribution of Working Group I to the Sixth Assessment Report of the Intergovernmental Panel on Climate Change*. Cambridge University Press.

Bauer, S. E., Ault, A., & Prather, K. A. (2013). Evaluation of aerosol mixing state classes in the GISS modelE-MATRIX climate model using single-particle mass spectrometry measurements. *Journal of Geophysical Research: Atmospheres*, *118*(17), 9834–9844. https://doi.org/10.1002/jgrd.50700

Bauer, S. E., Bausch, A., Nazarenko, L., Tsigaridis, K., Xu, B., Edwards, R., et al. (2013). Historical and future black carbon deposition on the three ice caps: Ice core measurements and model simulations from 1850 to 2100. *Journal of Geophysical Research: Atmospheres*, *118*(14), 7948–7961. https://doi.org/10.1002/jgrd.50612

Bauer, S. E., & Koch, D. (2005). Impact of heterogeneous sulfate formation at mineral dust surfaces on aerosol loads and radiative forcing in the Goddard Institute for Space Studies general circulation model. *Journal of Geophysical Research*, *110*(D17), D17202. https://doi.org/10.1029/2005JD005870

Bauer, S. E., Koch, D., Unger, N., Metzger, S. M., Shindell, D. T., & Streets, D. G. (2007). Nitrate aerosols today and in 2030: A global simulation including aerosols and tropospheric ozone. *Atmospheric Chemistry and Physics*, *7*(19), 5043–5059. https://doi.org/10.5194/acp-7-5043-2007

Bauer, S. E., & Menon, S. (2012). Aerosol direct, indirect, semidirect, and surface albedo effects from sector contributions based on the IPCC AR5 emissions for preindustrial and present-day conditions. *Journal of Geophysical Research*, *117*(D1), D01206. https://doi.org/10.1029/2011JD016816

Bauer, S. E., Menon, S., Koch, D., Bond, T. C., & Tsigaridis, K. (2010). A global modeling study on carbonaceous aerosol microphysical characteristics and radiative effects. *Atmospheric Chemistry and Physics*, *10*(15), 7439–7456. https://doi.org/10.5194/acp-10-7439-2010

Bauer, S. E., Mishchenko, M. I., Lacis, A. A., Zhang, S., Perlwitz, J., & Metzger, S. M. (2007). Do sulfate and nitrate coatings on mineral dust have important effects on radiative properties and climate modeling? *Journal of Geophysical Research*, *112*(D6), D06307. https://doi.org/10.1029/2005JD006977

Bauer, S. E., Tsigaridis, K., Faluvegi, G., Kelley, M., Lo, K. K., Miller, R. L., et al. (2020). Historical (1850–2014) aerosol evolution and role on climate forcing using the GISS ModelE2.1 contribution to CMIP6. *Journal of Advances in Modeling Earth Systems*, *12*(8), e2019MS001978. https://doi.org/10.1029/2019MS001978

Bauer, S. E., Tsigaridis, K., Faluvegi, G., Nazarenko, L., Miller, R. L., Kelley, M., & Schmidt, G. (2022). The turning point of the aerosol era [Dataset]. Goddard Space Flight Center. https://portal.nccs.nasa.gov/datashare/GISS/ModelE_tracers/papers/Bauer_et_al_2022/

Bauer, S. E., Tsigaridis, K., & Miller, R. (2016). Significant atmospheric aerosol pollution caused by world food cultivation. *Geophysical Research Letters*, *43*(10), 5394–5400. https://doi.org/10.1002/2016GL068354

Bauer, S. E., Wright, D. L., Koch, D., Lewis, E. R., McGraw, R., Chang, L.-S., et al. (2008). MATRIX (Multiconfiguration Aerosol TRacker of mIXing state): An aerosol microphysical module for global atmospheric models. *Atmospheric Chemistry and Physics*, *8*(20), 6003–6035. https://doi.org/10.5194/acp-8-6003-2008

Bell, M., Davis, D., & Fletcher, T. (2004). A retrospective assessment of mortality from the London smog episode of 1952: The role of influenza and pollution. *Environmental Health Perspectives*, *112*(1), 6–8. https://doi.org/10.1289/ehp.6539

Ceppi, P., Brient, F., Zelinka, M. D., & Hartmann, D. L. (2017). Cloud feedback mechanisms and their representation in global climate models. *WIREs Climate Change*, *8*(4), e465. https://doi.org/10.1002/wcc.465

Cesana, G., Del Genio, A. D., Ackerman, A. S., Kelley, M., Elsaesser, G., Fridlind, A. M., et al. (2019). Evaluating models' response of tropical low clouds to SST forcings using CALIPSO observations. *Atmospheric Chemistry and Physics*, *19*(5), 2813–2832. https://doi.org/10.5194/acp-19-2813-2019

Cesana, G. V., Ackerman, A. S., Fridlind, A. M., Silber, I., & Kelley, M. (2021). Snow reconciles observed and simulated phase partitioning and increases cloud feedback. *Geophysical Research Letters*, *48*(20), e2021GL094876. https://doi.org/10.1029/2021GL094876

Eyring, V., Bony, S., Meehl, G. A., Senior, C. A., Stevens, B., Stouffer, R. J., & Taylor, K. E. (2016). Overview of the Coupled Model Intercomparison Project Phase 6 (CMIP6) experimental design and organization. *Geoscientific Model Development*, *9*(5), 1937–1958. https://doi.org/10.5194/gmd-9-1937-2016

Feng, L., Smith, S. J., Braun, C., Crippa, M., Gidden, M. J., Hoesly, R., et al. (2020). The generation of gridded emissions data for CMIP6. *Geoscientific Model Development*, *13*(2), 461–482. https://doi.org/10.5194/gmd-13-461-2020

Forster, P., Storelvmo, T., Armour, K., Collins, W., Dufresne, J.-L., Frame, D., et al. (2021). The Earth's energy budget, climate feedbacks, and climate sensitivity. In V. Masson-Delmotte, P. Zhai, A. Pirani, S. L. Connors, C. Péan, S. Berger, et al. (Eds.), *Climate Change 2021: The Physical Science Basis. Contribution of Working Group I to the Sixth Assessment Report of the Intergovernmental Panel on Climate Change*. Cambridge University Press.

Gery, M. W., Whitten, G. Z., Killus, J. P., & Dodge, M. C. (1989). A photochemical kinetics mechanism for urban and regional scale computer modeling. *Journal of Geophysical Research*, *94*(D10), 12925. https://doi.org/10.1029/JD094iD10p12925

Ghan, S. J. (2013). Technical note: Estimating aerosol effects on cloud radiative forcing. *Atmospheric Chemistry and Physics*, *13*(19), 9971–9974. https://doi.org/10.5194/acp-13-9971-2013

Gidden, M. J., Riahi, K., Smith, S. J., Fujimori, S., Luderer, G., Kriegler, E., et al. (2019). Global emissions pathways under different socio-economic scenarios for use in CMIP6: A dataset of harmonized emissions trajectories through the end of the century. *Geoscientific Model Development*, *12*(4), 1443–1475. https://doi.org/10.5194/gmd-12-1443-2019

Guenther, A. B., Zimmerman, P. R., Harley, P. C., Monson, R. K., & Fall, R. (1993). Isoprene and monoterpene emission rate variability: Model evaluations and sensitivity analyses. *Journal of Geophysical Research*, *98*(D7), 12609–12617. https://doi.org/10.1029/93JD00527

Hansen, J. E., Sato, M., Lacis, A., Ruedy, R., Tegen, I., & Matthews, E. (1998). Climate forcings in the industrial era. *Proceedings of the National Academy of Sciences*, *95*(22), 12753–12758. https://doi.org/10.1073/pnas.95.22.12753

Hausfather, Z., Marvel, K., Schmidt, G. A., Nielsen-Gammon, J. W., & Zelinka, M. (2022). Climate simulations: Recognize the 'hot model' problem. *Nature*, *605*(7908), 26–29. https://doi.org/10.1038/d41586-022-01192-2

Hegerl, G. C., Brönnimann, S., Schurer, A., & Cowan, T. (2018). The early 20th century warming: Anomalies, causes, and consequences. *WIREs Climate Change*, *9*(4), e522. https://doi.org/10.1002/wcc.522

Hoesly, R. M., Smith, S. J., Feng, L., Klimont, Z., Janssens-Maenhout, G., Pitkanen, T., et al. (2018). Historical (1750–2014) anthropogenic emissions of reactive gases and aerosols from the Community Emissions Data System (CEDS). *Geoscientific Model Development*, *11*(1), 369–408. https://doi.org/10.5194/gmd-11-369-2018

Kelley, M., Schmidt, G. A., Nazarenko, L. S., Bauer, S. E., Ruedy, R., Russell, G. L., et al. (2020). GISS-E2.1: Configurations and climatology. *Journal of Advances in Modeling Earth Systems*, *12*(8), e2019MS002025. https://doi.org/10.1029/2019MS002025

Koch, D., Schmidt, G. A., & Field, C. V. (2006). Sulfur, sea salt, and radionuclide aerosols in GISS ModelE. *Journal of Geophysical Research*, *111*(D6), D06206. https://doi.org/10.1029/2004JD005550

Kok, J. F., Ridley, D. A., Zhou, Q., Miller, R. L., Zhao, C., Heald, C. L., et al. (2017). Smaller desert dust cooling effect estimated from analysis of dust size and abundance. *Nature Geoscience*, *10*(4), 274–278. https://doi.org/10.1038/ngeo2912

Lenssen, N. J. L., Schmidt, G. A., Hansen, J. E., Menne, M. J., Persin, A., Ruedy, R., & Zyss, D. (2019). Improvements in the GISTEMP uncertainty model. *Journal of Geophysical Research: Atmospheres*, *124*(12), 6307–6326. https://doi.org/10.1029/2018JD029522

Lewis, E. R., & Schwartz, S. E. (2013). Sea salt aerosol production fluxes: Estimates and critical analysis. In *Sea salt aerosol production: Mechanisms, methods, measurements and models* (pp. 299–344). American Geophysical Union. https://doi.org/10.1002/9781118666050.ch5

Liu, P., Kaplan, J. O., Mickley, L. J., Li, Y., Chellman, N. J., Arienzo, M. M., et al. (2021). Improved estimates of preindustrial biomass burning reduce the magnitude of aerosol climate forcing in the Southern Hemisphere. *Science Advances*, *7*(22), eabc1379. https://doi.org/10.1126/sciadv.abc1379

Lund, M. T., Aamaas, B., Stjern, C. W., Klimont, Z., Berntsen, T. K., & Samset, B. H. (2020). A continued role of short-lived climate forcers under the Shared Socioeconomic Pathways. *Earth System Dynamics*, *11*(4), 977–993. https://doi.org/10.5194/esd-11-977-2020

Meinshausen, M., Nicholls, Z. R. J., Lewis, J., Gidden, M. J., Vogel, E., Freund, M., et al. (2020). The shared socio-economic pathway (SSP) greenhouse gas concentrations and their extensions to 2500. *Geoscientific Model Development*, *13*(8), 3571–3605. https://doi.org/10.5194/gmd-13-3571-2020

Menon, S., Koch, D., Beig, G., Sahu, S., Fasullo, J., & Orlikowski, D. (2010). Black carbon aerosols and the third polar ice cap. *Atmospheric Chemistry and Physics*, *10*(10), 4559–4571. https://doi.org/10.5194/acp-10-4559-2010

Menon, S., & Rotstayn, L. (2006). The radiative influence of aerosol effects on liquid-phase cumulus and stratiform clouds based on sensitivity studies with two climate models. *Climate Dynamics*, *27*(4), 345–356. https://doi.org/10.1007/s00382-006-0139-3

Menon, S., Unger, N., Koch, D., Francis, J., Garrett, T., Sednev, I., et al. (2008). Aerosol climate effects and air quality impacts from 1980 to 2030. *Environmental Research Letters*, *3*(2), 024004. https://doi.org/10.1088/1748-9326/3/2/024004

Metzger, S., Dentener, F., Pandis, S., & Lelieveld, J. (2002). Gas/aerosol partitioning: 1. A computationally efficient model. *Journal of Geophysical Research*, *107*(D16), ACH 16-1-ACH 16-24. https://doi.org/10.1029/2001JD001102

Miller, R. L., Cakmur, R. V., Perlwitz, J., Geogdzhayev, I. V., Ginoux, P., Koch, D., et al. (2006). Mineral dust aerosols in the NASA Goddard Institute for Space Sciences ModelE atmospheric general circulation model. *Journal of Geophysical Research*, *111*(D6), D06208. https://doi.org/10.1029/2005JD005796

Miller, R. L., Schmidt, G. A., Nazarenko, L. S., Bauer, S. E., Kelley, M., Ruedy, R., et al. (2021). CMIP6 historical simulations (1850–2014) with GISS-E2.1. *Journal of Advances in Modeling Earth Systems*, *13*(1), e2019MS002034. https://doi.org/10.1029/2019MS002034

Miller, R. L., Schmidt, G. A., Nazarenko, L. S., Tausnev, N., Bauer, S. E., DelGenio, A. D., et al. (2014). CMIP5 historical simulations (1850–2012) with GISS ModelE2. *Journal of Advances in Modeling Earth Systems*, *6*(2), 441–478. https://doi.org/10.1002/2013MS000266

Mortier, A., Gliß, J., Schulz, M., Aas, W., Andrews, E., Bian, H., et al. (2020). Evaluation of climate model aerosol trends with ground-based observations over the last 2 decades – An AeroCom and CMIP6 analysis. *Atmospheric Chemistry and Physics*, *20*(21), 13355–13378. https://doi.org/10.5194/acp-20-13355-2020

Myhre, G., Aas, W., Cherian, R., Collins, W., Faluvegi, G., Flanner, M., et al. (2017). Multi-model simulations of aerosol and ozone radiative forcing due to anthropogenic emission changes during the period 1990–2015. *Atmospheric Chemistry and Physics*, *17*(4), 2709–2720. https://doi.org/10.5194/acp-17-2709-2017

Nazarenko, L. S., Tausnev, N., Russell, G. L., Rind, D., Miller, R. L., Schmidt, G. A., et al. (2022). Future climate change under SSP emission scenarios with GISS-E2.1. *Journal of Advances in Modeling Earth Systems*, *14*(7), e2021MS002871. https://doi.org/10.1029/2021MS002871

O'Neill, B. C., Tebaldi, C., van Vuuren, D. P., Eyring, V., Friedlingstein, P., Hurtt, G., et al. (2016). The Scenario Model Intercomparison Project (ScenarioMIP) for CMIP6. *Geoscientific Model Development*, *9*(9), 3461–3482. https://doi.org/10.5194/gmd-9-3461-2016

Quaas, J., Jia, H., Smith, C., Albright, A. L., Aas, W., Bellouin, N., et al. (2022). Robust evidence for reversal in the aerosol effective climate forcing trend. *Atmospheric Chemistry and Physics Discussions*, *22*(18), 12221–12239. https://doi.org/10.5194/acp-2022-295

Raghuraman, S. P., Paynter, D., & Ramaswamy, V. (2021). Anthropogenic forcing and response yield observed positive trend in Earth's energy imbalance. *Nature Communications*, *12*(1), 4577. https://doi.org/10.1038/s41467-021-24544-4

Ramachandran, S., Rupakheti, M., & Lawrence, M. G. (2020). Aerosol-induced atmospheric heating rate decreases over South and East Asia as a result of changing content and composition. *Scientific Reports*, *10*(1), 20091. https://doi.org/10.1038/s41598-020-76936-z

Shindell, D. T., Faluvegi, G., & Bell, N. (2003). Preindustrial-to-present-day radiative forcing by tropospheric ozone from improved simulations with the GISS chemistry-climate GCM. *Atmospheric Chemistry and Physics*, *3*(5), 1675–1702. https://doi.org/10.5194/acp-3-1675-2003

Shindell, D. T., Faluvegi, G., Unger, N., Aguilar, E., Schmidt, G. A., Koch, D. M., et al. (2006). Simulations of preindustrial, present-day, and 2100 conditions in the NASA GISS composition and climate model G-PUCCINI. *Atmospheric Chemistry and Physics*, *6*(12), 4427–4459. https://doi.org/10.5194/acp-6-4427-2006

Shindell, D. T., Grenfell, J. L., Rind, D., Grewe, V., & Price, C. (2001). Chemistry-climate interactions in the Goddard Institute for Space Studies general circulation model: 1. Tropospheric chemistry model description and evaluation. *Journal of Geophysical Research*, *106*(D8), 8047–8075. https://doi.org/10.1029/2000JD900704

Struthers, H., Ekman, A., Glantz, P., Iversen, T., Kirkevåg, A., Seland, Ø., et al. (2013). Climate-induced changes in sea salt aerosol number emissions: 1870 to 2100. *Journal of Geophysical Research*, *118*(2), 1–13. https://doi.org/10.1002/jgrd.50129

Subba, T., Gogoi, M. M., Pathak, B., Bhuyan, P. K., & Babu, S. S. (2020). Recent trend in the global distribution of aerosol direct radiative forcing from satellite measurements. *Atmospheric Science Letters*, *21*(11), e975. https://doi.org/10.1002/asl.975

Tang, I. N., & Munkelwitz, H. R. (1994). Aerosol phase transformation and growth in the atmosphere. *Journal of Applied Meteorology*, *33*(7), 791–796. https://doi.org/10.1175/1520-0450(1994)033<0791:APTAGI>2.0.CO;2

Tsigaridis, K., Daskalakis, N., Kanakidou, M., Adams, P. J., Artaxo, P., Bahadur, R., et al. (2014). The AeroCom evaluation and intercomparison of organic aerosol in global models. *Atmospheric Chemistry and Physics*, *14*(19), 10845–10895. https://doi.org/10.5194/acp-14-10845-2014

Tsigaridis, K., & Kanakidou, M. (2007). Secondary organic aerosol importance in the future atmosphere. *Atmospheric Environment*, *41*(22), 4682–4692. https://doi.org/10.1016/j.atmosenv.2007.03.045

Tsigaridis, K., & Kanakidou, M. (2018). The present and future of secondary organic aerosol direct forcing on climate. *Current Climate Change Reports*, *4*(2), 84–98. https://doi.org/10.1007/s40641-018-0092-3

Tsigaridis, K., Koch, D., & Menon, S. (2013). Uncertainties and importance of sea spray composition on aerosol direct and indirect effects. *Journal of Geophysical Research: Atmospheres*, *118*(1), 220–235. https://doi.org/10.1029/2012JD018165

Turnock, B. J. (2016). *Public health: What it is and how it works*. Jones & Bartlett Publishers.

Twomey, S. (1977). The influence of pollution on the shortwave albedo of clouds. *Journal of the Atmospheric Sciences*, *34*(7), 1149–1152. https://doi.org/10.1175/1520-0469(1977)034<1149:TIOPOT>2.0.CO;2

van der Werf, G. R., Randerson, J. T., Giglio, L., van Leeuwen, T. T., Chen, Y., Rogers, B. M., et al. (2017). Global fire emissions estimates during 1997–2016. *Earth System Science Data*, *9*(2), 697–720. https://doi.org/10.5194/essd-9-697-2017

van Marle, M. J. E., Kloster, S., Magi, B. I., Marlon, J. R., Daniau, A.-L., Field, R. D., et al. (2017). Historic global biomass burning emissions for CMIP6 (BB4CMIP) based on merging satellite observations with proxies and fire models (1750–2015). *Geoscientific Model Development*, *10*(9), 3329–3357. https://doi.org/10.5194/gmd-10-3329-2017

Vehkamäki, H., Kulmala, M., Napari, I., Lehtinen, K. E. J., Timmreck, C., Noppel, M., & Laaksonen, A. (2002). An improved parameterization for sulfuric acid–water nucleation rates for tropospheric and stratospheric conditions. *Journal of Geophysical Research*, *107*(D22), AAC 3-1–AAC 3-10. https://doi.org/10.1029/2002JD002184

Yang, Y., Wang, H., Smith, S. J., Zhang, R., Lou, S., Yu, H., et al. (2018). Source apportionments of aerosols and their direct radiative forcing and long-term trends over continental United States. *Earth's Future*, *6*(6), 793–808. https://doi.org/10.1029/2018EF000859

Zelinka, M. D., Myers, T. A., McCoy, D. T., Po-Chedley, S., Caldwell, P. M., Ceppi, P., et al. (2020). Causes of higher climate sensitivity in CMIP6 models. *Geophysical Research Letters*, *47*(1), e2019GL085782. https://doi.org/10.1029/2019GL085782

Zhao, B., Jiang, J. H., Gu, Y., Diner, D., Worden, J., Liou, K.-N., et al. (2017). Decadal-scale trends in regional aerosol particle properties and their linkage to emission changes. *Environmental Research Letters*, *12*(5), 054021. https://doi.org/10.1088/1748-9326/aa6cb2